Adaptive multiscale extended finite element method (MS-XFEM) for the simulation of multiple fractures propagation in geological formations

Xu, Fanxiang; Hajibeygi, Hadi; Sluys, Lambertus J.

DOI
10.1016/j.jcp.2023.112114

Publication date
2023

Document Version
Final published version

Published in
Journal of Computational Physics

Citation (APA)
Xu, F., Hajibeygi, H., & Sluys, L. J. (2023). Adaptive multiscale extended finite element method (MS-XFEM) for the simulation of multiple fractures propagation in geological formations. *Journal of Computational Physics*, *486*, Article 112114. https://doi.org/10.1016/j.jcp.2023.112114

Journal of Computational Physics 486 (2023) 112114

Contents lists available at ScienceDirect

Journal of Computational Physics

journal homepage: www.elsevier.com/locate/jcp

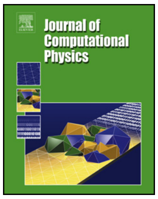

Adaptive multiscale extended finite element method (MS-XFEM) for the simulation of multiple fractures propagation in geological formations

Fanxiang Xu [a,*], Hadi Hajibeygi [b], Lambertus J. Sluys [a]

[a] *Department of Materials, Mechanics, Management and Design, Delft University of Technology, Delft, 2600GA, the Netherlands*
[b] *Department of Geoscience and Engineering, Delft University of Technology, Delft, 2600GA, the Netherlands*

ARTICLE INFO

Article history:
Received 28 November 2022
Received in revised form 2 March 2023
Accepted 29 March 2023
Available online 5 April 2023

Keywords:
Fracture propagation
Multiscale extended finite element method
Geomechanics
Scalable iterative solver

ABSTRACT

In fractured geological formations, as a result of the in-situ stress changes, fractures can propagate or slide. This phenomenon can be efficiently modeled by the extended finite element method (XFEM) when there are only a few fractures present. However, geological reservoirs contain many fractures which can also cross and are densely populated. Therefore, the classical XFEM is too expensive to be applied for the simulation of propagating fractures in geological formations. To reduce the costs, typically, homogenization or upscaling is used. However, they result in inaccurate solutions, since no separation of scales exists in this process. To resolve this challenge, in this work, a multiscale XFEM (MS-XFEM) for propagating fractures is developed and presented. In each time step, given the current geometries of the fractures, local XFEM-based basis functions are constructed or adaptively updated. The adaptive update takes place in certain regions where fracture geometries are changed due to propagation. Using these basis functions, a very efficient FEM-based coarse-scale system is developed since it has no extra degrees of freedom (DOFs). Once the coarse-scale system is solved, its solution is prolonged to the fine-scale original resolution using the basis functions. This approximate fine-scale solution is then used to estimate the group of growing fractures tips and their growing angles. This allows for exploiting the locality of the propagation process fully while solving a global system. To control the error, an iterative procedure is also developed. Proof-of-concept test cases are presented to study the developed MS-XFEM algorithm. It is shown that MS-XFEM results are capable of predicting the propagating paths for complicated fracture patterns. As such, MS-XFEM casts a promising method for field-scale applications.

1. Introduction

The equilibrium state of fractured geological formations can be violated due to a sudden change of the state of stress, which can arise from anthropological operations. As a consequence, fractures can be activated and then slide or even propagate. The consequences of sliding fracture phenomena can be disastrous, as it may cause surface subsidence or induced earthquakes [1,2], and impose high risks to the safety of the residents and surface infrastructure [3]. To be able to control and alleviate these risks, accurate and efficient simulation of growing fractures in underground formations is crucial.

---

[*] Corresponding author.
E-mail addresses: f.xu-4@tudelft.nl (F. Xu), H.Hajibeygi@tudelft.nl (H. Hajibeygi), L.J.Sluijs@tudelft.nl (L.J. Sluys).

https://doi.org/10.1016/j.jcp.2023.112114

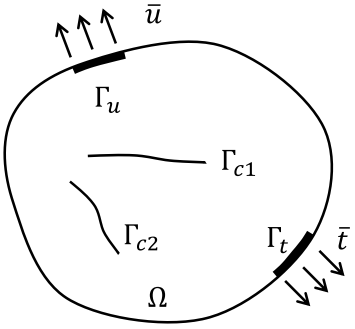

Fig. 1. An illustration of fractured domain setup.

In view of fracture growth, many mechanical theories have been proposed. To determine whether a fracture tip can grow or not, the Griffith theory [4] is commonly used. To further track the growth direction, different theories have been applied. The maximum principle stress theory [5] has been proved to be able to track the direction of crack growth under tension accurately. For complicated fracture networks, or a multiple fractured system, some fractures tips may not grow even if they meet the Griffith criterion as the global system tends to release minimum energy and form a stable crack pattern. The double virtual incremental method is a good option to determine whether the group of tips should propagate [6,7].

To simulate growing fractures, the extended finite element method (XFEM) [8,9], which is an embedded method for fracture mechanics simulation, is a viable option. Unlike the unstructured grid approach [10–15], the embedded method overcomes the problem of remeshing. It implies the enrichment to shape functions meanwhile not interfering with the discretization layout [16–20,9,21–26]. To match the partition of unity (PoU) property of shape functions [27], extra degrees of freedom (DOFs) are given to enriched nodes. Level set functions are introduced to help XFEM track the fracture tip positions [28,29].

Being widely used in fracture mechanics, the classical XFEM is not the ideal method for the simulation of massive DOFs propagation in geological formations. It is efficient to apply homogenization or an upscaling strategy using XFEM with coarse grid sizes but this will lead to loss of accuracy [30–38] and possibly even the wrong prediction of propagation paths of fractures. In addition to that, homogenization of the heterogeneities that span over large length scales can cause the loss of details. However, a finer mesh is computationally expensive even if it can preserve the accuracy of the final solution. The number of extra DOFss will increase significantly as the finer mesh is paired with XFEM for multiple fractures simulation, which makes the linear system size too large to be computed efficiently.

A scalable simulator, or a multiscale strategy, is used to seek the good balance between efficiency and accuracy for the simulation of the propagation of complicated fracture networks. The multiscale method (MS) [39–48] has been proved to be able to capture the fine-scale heterogeneity, by constructing accurate coarse-scale systems and thus reduce the computational costs. In presence of fractures that span over different length scales, an adaptive local projection method has been developed [49,50]. This method requires to solve on the coarse mesh and the coarse scale mesh solution is used as the boundary condition to simulate the micro-scale cracks DOFs on a finer scale mesh. As for the more geoscience oriented method, the multiscale extended finite element method (MS-XFEM) has been recently developed by Xu et al. [51]. This method incorporates the fine scale discontinuities into the basis functions and creates a finite element type problem on the coarse-scale mesh which contains no extra DOFs. Computation only takes place on a coarse scale mesh.

This paper expands the MS-XFEM to simulate fracture growth in highly fractured formations. The growing fracture tips are tracked by updating the basis functions which are generated based on the revised fine-scale stiffness matrix in an algebraic manner. Thus, in each time step the basis functions are updated only at the local domains in which the fracture geometry will change. Still, no extra DOFs are introduced on the coarse scale system. Preconditioned GMRES is used during the iterative solving stage to control the accuracy of the final results.

The structure of this paper is set as follows. First, the governing equations and the fine scale XFEM method are introduced. Next, the level set functions assisted XFEM in simulation of multiple fractures propagation is introduced. Then the principles of how MS-XFEM in simulation of multiple DOFs simulation is presented. Different numerical test cases are presented to demonstrate the performance of the new method.

2. Governing equations and XFEM

Consider a domain Ω bounded by Γ as shown in Fig. 1. Prescribed displacements or Dirichlet boundary condition are imposed on Γ_u, while traction are imposed on Γ_t. The multiple crack surfaces $\Gamma_{c,i=1\ldots n}$ are assumed to be traction-free under tension loading.

The momentum balance equations and boundary conditions read

$$\nabla \cdot \sigma + f = 0 \quad in\, \Omega, \tag{1}$$

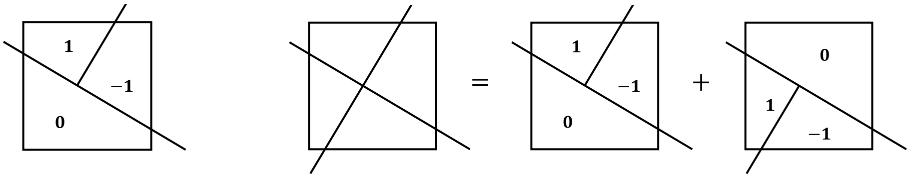

(a) (b)

Fig. 2. Two types of the junction enrichment functions (a) T-shape junction enrichment functions. (b) X-shape junction enrichment divided into two T-shape enrichment functions.

$$\sigma \cdot n = \bar{t} \quad on\ \Gamma_t, \tag{2}$$

$$\sigma \cdot n = 0 \quad on\ \Gamma_c, \tag{3}$$

$$u = \bar{u} \quad on\ \Gamma_u, \tag{4}$$

where σ is the stress tensor and u is the displacement field over the whole domain. n is the normal vector pointing outside the domain.

A linear elastic constitutive law is applied in this paper. The second order partial differential equation (PDE) for displacement field u reads

$$\nabla \cdot (\mathbf{C} : \nabla^s u) + f = 0, \tag{5}$$

where ∇^s denotes the symmetrical part of the gradient operator. **C** is the linear elastic constitutive tensor. In this manuscript, the constitutive law is simplified to the linear elastic model without considering the poroelasticity. However, a damage model or poroelasticity model can be conveniently integrated in Eq. (5) [52,53,41]. Eq. (5) is then solved for computational domains with DOFs (representing faults and fractures) by using XFEM. Next, the XFEM is revisited briefly.

2.1. Extended Finite Element Method (XFEM)

The XFEM introduces different types of enrichment to the classic shape functions to represent discontinuities. The element cut fully by the fracture path is enriched by a jump enrichment. Elements crossed by different fractures are enriched with a junction enrichment. An additional crack tip enrichment is not applied in this paper for convenience of implementation. Below brief descriptions of the two enrichment functions are provided.

2.1.1. Jump enrichment

The jump enrichment represents the discontinuity in the displacement field across the fractured body. The jump enrichment is often chosen as a step function, which can be expressed as

$$H(x) = \begin{cases} 1 & \text{on } \Omega^+ \\ -1 & \text{on } \Omega^- \end{cases}. \tag{6}$$

Note that Ω^+ and Ω^- zones are determined based on the normal vector n pointing out of the fracture curve.

2.1.2. Junction enrichment

In a multiple DOFs simulation, crossing of DOFs needs to be considered. To simulate that in XFEM, the junction enrichment, or the crossing enrichment, is applied [25]. There are two situations of crossing considered: T-shape crossing and X-shape crossing.

The T-shape enrichment is the commonly seen scenario in an underground fracture network and it is illustrated in Fig. 2(a). The crack with its tip joined with another crack's main path is called the minor crack and the other crack is called the main crack. For any Gauss point in the T-shape crossed element there is one jump function addressed due to the major crack. If this Gauss point is on the negative side of the main crack, i.e., the jump function value due to main crack $H_I(x)$ is negative, the junction enrichment function value is 0. If this point is on the positive side of the main crack, i.e., the jump function value due to main crack $H_I(x)$ is positive, the junction enrichment function value is equal to the jump enrichment function value due to the minor crack $H_{II}(x)$. Thus T-shape function $J(x)$ is given by

$$J(x) = \begin{cases} H_{II}(x) & H_I(x) > 0 \\ 0 & H_I(x) < 0 \end{cases}. \tag{7}$$

Another type of crossing is X-shape crossing as shown in Fig. 2(b). To enrich this, usually the minor crack is decomposed into two minor DOFs. Thus, two sets of T-shape functions are introduced to each of the X-shape enriched node. Note that for either T-shape or X-shape junction enrichment, there will be always a jump enrichment added to each junction enriched node due to the main crack.

2.1.3. XFEM linear system

The XFEM approximates the displacement field d at fine-scale resolution h by d^h which is defined as

$$d \approx d^h = \sum_{i \in I} u_i N_i + \sum_{j \in J} a_j N_j (H(x) - H(x_c)) + \sum_{k \in K} b_k N_k (J(x) - J(x_c)), \tag{8}$$

where N, H and J represent, respectively, the classical FEM shape functions, the jump function and the junction enrichment functions. x_c represents the coordinates of the enriched mesh nodes. The u denotes the standard DOFs associated to the classical finite element method and a denotes the extra DOFs associated to the jump enriched nodes. Note that a also includes the jump enriched extra DOFs in the crossing fractured element due to the main crack. The multipliers b are the extra DOFs due to the junction enrichment. The resulting linear system entails the nodal displacement unknowns u, as well as the jump enriched extra DOFs a and junction enriched extra DOFs b per fracture (and fault). The augmented XFEM linear system $K^h\ d^h = f^h$, therefore, reads

$$\underbrace{\begin{bmatrix} K_{uu} & K_{ua} & K_{ub} \\ K_{au} & K_{aa} & K_{ab} \\ K_{bu} & K_{ba} & K_{bb} \end{bmatrix}}_{\mathbf{K^h}} \underbrace{\begin{bmatrix} u \\ a \\ b \end{bmatrix}}_{\mathbf{d^h}} = \underbrace{\begin{bmatrix} f_u \\ f_a \\ f_b \end{bmatrix}}_{\mathbf{f^h}}. \tag{9}$$

3. Multiple fractures propagation simulation

In this section, the methodology used to predict fracture propagation is explained. To simulate fractures growth, level sets functions assisted XFEM is introduced. The same methodology is used during the application of MS-XFEM in the simulation of fracture propagation.

3.1. Propagation criterion

Griffith's theory [4] states that the fracture tip will grow if the energy release rate, G, is larger than or equal to the critical energy release rate, G_c. This is expressed as

$$G \geqslant G_c, \tag{10}$$

where G is defined as the rate of energy decreased per unit fracture surface area increased [4]. Eq. (10) can be also written in terms of the stress intensity factor K as

$$K \geqslant K_c, \tag{11}$$

where K_c is called fracture toughness.

The fracture increment in this paper is defined as a user-defined input. The angle of propagation can be quantified using different theories. In this paper, only test cases under tensile forces are performed, the maximum principle stress theory is used to predict the direction of fracture propagation according to

$$\theta = 2 \arctan \frac{1}{4} (\frac{K_I}{K_{II}} \pm \sqrt{(\frac{K_I}{K_{II}})^2 + 8}), \tag{12}$$

where K_I is the stress intensity factor for mode I fracture which means the opening mode fracture and K_{II} is the stress intensity factor for mode II fracture which represents the sliding mode fracture.

3.2. Level sets functions assisted fracture propagation

The growing crack tip always leads to a change of crack geometries, which can be tracked by using level sets functions. Below the level sets functions and how they can help track the propagation of fractures tips will be introduced briefly.

3.2.1. Level sets functions

Level set functions are usually defined as signed distance functions. Two level set functions are applied in this paper. The first function, ψ, represents the signed distance from any point to the main crack path. It is defined as

$$\psi(x,t) = \pm \min_{x^{\Gamma_c} \in \Gamma_c} ||(x - x^{\Gamma_c})||. \tag{13}$$

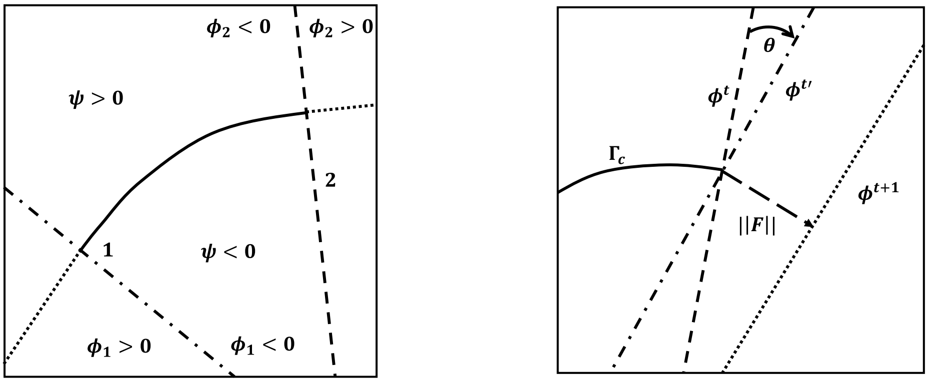

(a) (b)

Fig. 3. Illustration of (a) the level set functions and (b) the update of the function ϕ upon a crack increment $||F||$.

Γ_c represents the crack or discontinuity interface and thus it is a zero valued interface for ψ. The second function, ϕ, is defined as the signed distance to the tangential line ξ crossing the crack tip, defined as

$$\phi_i(x,t) = \pm \min_{x^\xi \in \xi, i} ||(x - x^\xi)||, \quad i = 1, 2. \tag{14}$$

Similarly, ξ represents the zero valued interface for function ϕ. Normally, there will be two ϕ functions indicating that there are two tips for each crack. To combine them into one function, for any point the maximum value of $[\phi_1, \phi_2]$ is selected as the ϕ value, i.e.,

$$\phi(x,t) = \max(\phi_1, \phi_2). \tag{15}$$

In Fig. 3 (a) the two level set functions are shown.

3.2.2. Update of level sets functions

The update of level sets functions is done at the beginning of each step. The crack angle can be computed using Eq. (12). The incremental crack length is also explicitly known as user-defined input and its value is denoted as $||\mathbf{F}||$. The growth of the tip is then traced by updating the zero value interface of function ϕ with propagation speed $\mathbf{F} = (F_x, F_y)$.

The current functions ϕ at time step, ϕ^t, are rotated with angle θ as shown in Fig. 3 (b). The function $(\phi^t)'$ represents the rotated function ϕ^t. Next, function ϕ^{t+1} is constructed via

$$\phi^{t+1} = (\phi^t)' - ||\mathbf{F}||. \tag{16}$$

After updating functions ϕ, the function ψ is recomputed to construct the function ψ^{t+1}. Details can be found in the literature [29].

Updating the level set function values is not necessarily needed for all the elements in the model. The level set functions update can be limited to the elements, or to a narrow band, in which the fracture tips will propagate into.

3.3. Multiple fractures propagation

Unlike propagation of a single fracture, the impact of the increment of one fracture tip to another needs also to be considered in a multiple fractures propagation problem. Some fracture tips will grow and they are grouped as competitive tips n_{comp}. These tips must strictly follow Eq. (11). But not all of them can grow since the whole fractured system tends to form a stable crack pattern with minimum energy dissipation [6]. The unstable configuration of fractures path is defined as

$$\left(\frac{\partial G_i}{\partial l_j} - \frac{\partial G_{c,i}}{\partial l_j}\right) \geqslant 0, \quad \forall i, j \in n_{comp}, \tag{17}$$

where $\partial G_i/\partial l_j$ is the derivative of energy release rate of crack tip i with respect to crack tip j increment. $\partial G_{c,i}/\partial l_j$ is the derivative of critical energy release rate of crack tip i with respect to crack tip j increment.

At the beginning of each fracture growth step, the matrix $\partial G/\partial l$ needs to be constructed to check whether the chosen growing path meets the criterion described by Eq. (17). The double virtual incremental method is applied to construct the matrix $\partial G/\partial l$. In the double virtual incremental method, it is assumed that the growth of the tips would only affect a small region near the fractures tips. The virtual fracture tip i increment, l_i, is approximated using virtual displacement function

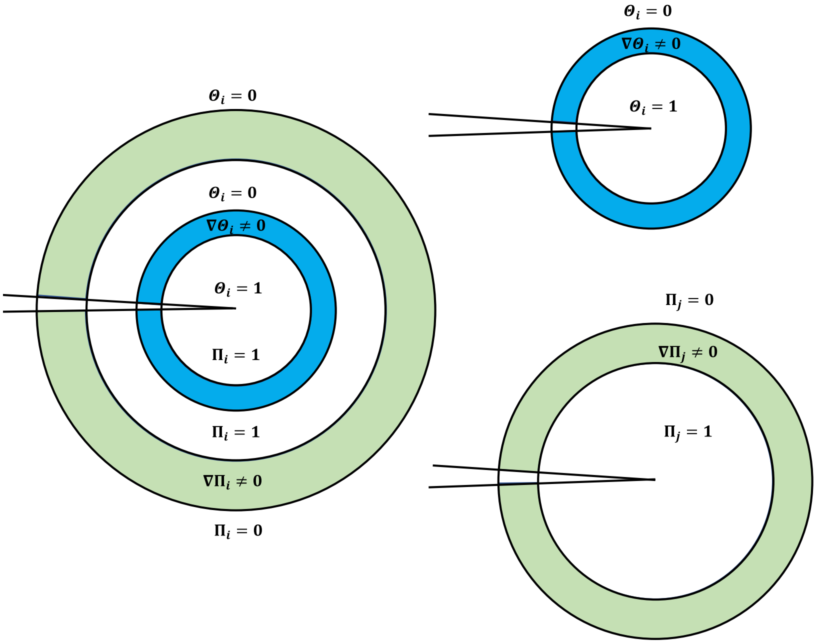

Fig. 4. Function Π (green) and function Θ (blue) belong to one tip ($i = j$) or belong to different tips ($i \neq j$). The gradients of both functions are 0 outside the colored zones. (For interpretation of the colors in the figure(s), the reader is referred to the web version of this article.)

Θ_i. The virtual fracture tip j increment, l_j, is approximated using the virtual displacement function Π_j. These functions are shown in Fig. 4. Note that the radius of the non-zero gradient zone of function Π is normally twice the radius of the none-zero gradient zone of function Θ.

The virtual displacement field $\tilde{\mathbf{d}}_j$ is constructed in order to compute $\partial G_i/\partial l_j$. To compute this virtual displacement field, a virtual force vector $\tilde{\mathbf{f}}_{\Pi_j}$ around the fracture tip j is defined as

$$\tilde{\mathbf{f}}_{\Pi_j} = \int \mathbf{B}^T(\mathbf{C}\tilde{\mathbf{B}}_{\Pi_j}\mathbf{d} - \sigma div(\Pi_j))d\Omega + \int \tilde{\mathbf{B}}^T_{\Pi_j}\sigma d\Omega, \tag{18}$$

where $\mathbf{C}$ is the linear elastic constitutive matrix. The B matrix represents the strain-displacement matrix that contains the gradients of shape functions inside each element [54]. The matrix $\tilde{\mathbf{B}}_{\Pi_j}$ is assembled similar to the construction of the $\mathbf{B}$ matrix. Each component of $\tilde{\mathbf{B}}_{\Pi_j}$ is constructed by multiplying the gradient of the function Π. Details can be found in [6]. The virtual displacement field $\tilde{\mathbf{d}}_j$ is given by

$$\tilde{\mathbf{d}}_j = \mathbf{K}^{-1}\tilde{\mathbf{f}}_{\Pi_j}. \tag{19}$$

The derivative of the energy release rate at fracture tip i corresponding to incremental of fracture tip j increment is computed using

$$\frac{\partial G_i}{\partial l_j} = \mathbf{d}^T[\int(\mathbf{B}^T\mathbf{C}\tilde{\mathbf{B}}_{\Theta_i} + \tilde{\mathbf{B}}^T_{\Theta_i}\mathbf{C}\mathbf{B} - \mathbf{B}^T\mathbf{C}\mathbf{B})d\Omega]\tilde{\mathbf{d}}^T_j. \tag{20}$$

The construction of $\tilde{\mathbf{B}}_{\Theta_i}$ is carried out by multiplying $\mathbf{B}$ with the gradient of function Θ.

The matrix $\partial G/\partial l$ is constructed by assembling the terms $\partial G_i/\partial l_j$. The maximum subdeterminant of matrix $\partial G/\partial l$ provides the set of fracture tips that would grow in the current time step, defined as N_{grow}, which read

$$N_{grow} = \underbrace{max}_{\forall i,j \in n_{comp}} \left[det(\frac{\partial G_i}{\partial l_j}) \geqslant 0\right]. \tag{21}$$

If the maximum subdeterminant value is negative, no fracture tips will grow.

4. MS-XFEM in simulation of multiple fractures propagation

The propagation of a fracture network, unlike propagation of a single fracture, means that many more extra DOFs are added in each new time step. This will increase the size of additional blocks such as K_{aa} shown in (9). Multiscale simulation

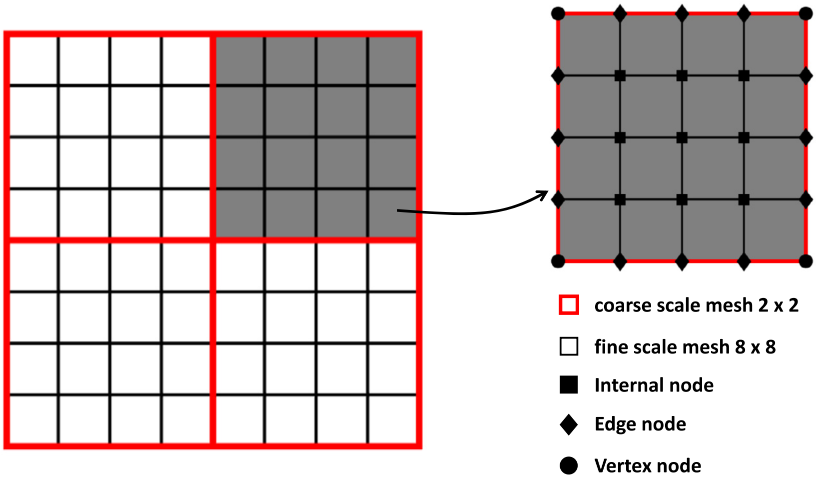

Fig. 5. Illustration of the multiscale mesh imposed on a given fine-scale mesh, with a coarsening ratio of 4 × 4. The fine scale mesh nodes in each coarse scale element can be categorized as internal nodes, edge nodes and vertex nodes.

becomes necessary to reduce the computational burden caused by the excessive number of fractures. MS-XFEM is creating a finite element type system on a coarse scale mesh without any extra DOFs required. It would become a good solution to simulate the fractures propagation in underground formation. Preconditioned GMRES is used to control the error level in the final solution as will be explained.

4.1. Multiscale simulation

The fine scale solution $\mathbf{d}^h$ can be approximated with the solution field $\mathbf{d}'^h$ by a multiscale formulation

$$\mathbf{d}^h \approx \mathbf{d}'^h = \mathbf{P}\,\mathbf{d}^H, \tag{22}$$

where $\mathbf{P}$ is the matrix of basis functions (i.e., prolongation operator) and $\mathbf{d}^H$ are the nodal displacements at the coarse scale mesh Ω^H. Prolongation operator $\mathbf{P}$ has the dimension of $N^h \times N^H$. N^h is the size of the fine-scale enriched XFEM system including the extra DOFs and N^H is the size of the coarse mesh. All extra DOFs and enrichment functions are included in matrix $\mathbf{P}$ instead of vector $\mathbf{d}^H$, which reduces the size of the coarse scale linear system. This is crucial in significantly improving the computational efficiency in these large-scale heterogeneous systems.

4.1.1. Coarse scale linear system

MS-XFEM solves the linear system of equations on the coarse mesh, imposed on a given fine-scale mesh, as shown in Fig. 5. The coarsening ratio is defined as the ratio between the coarse mesh size and fine-scale mesh size, which is 4 × 4 for the example shown in Fig. 5.

To construct the coarse-scale system of equations and solve for $\mathbf{d}^H$, the fine-scale linear system ($\mathbf{K}^h\ \mathbf{d}^h = \mathbf{f}^h$) is restricted to the coarse-scale via

$$\underbrace{(\mathbf{R}\,\mathbf{K}^h\ \mathbf{P})}_{\mathbf{K}^H}\ \mathbf{d}^H = \mathbf{R}\,\mathbf{f}^h. \tag{23}$$

Here, $\mathbf{R}$ is the restriction operator with size $N^H \times N^h$, defined as the transpose of basis function operator

$$\mathbf{R} = \mathbf{P}^T. \tag{24}$$

This results in the coarse-scale system matrix $\mathbf{K}^H$ size of $N^H \times N^H$. Once the coarse-scale system is solved on $\mathbf{K}^H$ space for $\mathbf{d}^H$, one can compute the approximate fine-scale solution using Eq. (22). Overall, the multiscale procedure can be summarized as finding an approximate solution $\mathbf{d}'^h$ according to

$$\mathbf{d}^h \approx \mathbf{d}'^h = \mathbf{P}\,\mathbf{d}^H = \mathbf{P}(\mathbf{R}\,\mathbf{K}^h\ \mathbf{P})^{-1}\mathbf{R}\,\mathbf{f}^h. \tag{25}$$

In here, the term $\mathbf{P}(\mathbf{R}\,\mathbf{K}^h\ \mathbf{P})^{-1}\mathbf{R}$ is called the multiscale operator $\mathbf{M}_{\mathbf{MS}}^{\mathbf{-1}}$.

Next, the prolongation operator $\mathbf{P}$, i.e., the basis functions are explained in detail. Once $\mathbf{P}$ is known, all terms in Eq. (25) are defined.

4.1.2. Iterative strategy

Preconditioned GMRES [55] is applied to control the error and reduce it to any desired tolerance. To reduce the high frequency error, a fine-scale smoother $\mathbf{M}_{sm}^{-1}$ (usually named as ILU(0) [56]) is paired with the multiscale operator $\mathbf{M}_{MS}^{-1}$. The preconditioner used here involves the multiscale operator and the fine scale smoothing operator following

$$\mathbf{M}^{-1} = \mathbf{M}_{MS}^{-1} + \mathbf{M}_{sm}^{-1}(I - K^h\, \mathbf{M}_{MS}^{-1}). \tag{26}$$

The system in Eq. (25) is then iteratively solved using preconditioned GMRES until the error is reduced to the desired tolerance.

4.2. Algebraically construction of basis functions

In order to obtain the basis functions, a local XFEM problem can be solved in each coarse element of Ω^H. This can be expressed as

$$\nabla \cdot (C : (\nabla^S N_i^H)) = 0 \quad \text{in } \Omega^H, \tag{27}$$

subject to local boundary conditions. A reduced-dimensional equilibrium equation is composed to solve for the boundary elements as

$$\nabla_{\parallel} \cdot (C_r : (\nabla_{\parallel}^S N_i^H)) = 0 \quad \text{on } \Gamma^H. \tag{28}$$

Here, Γ^H denotes the boundary of the coarse element Ω^H. In addition, $\nabla_{\parallel}^S$ denotes the reduced dimensional divergence and symmetrical gradient operators, which contains the gradient to either only x-direction or only y-direction. Moreover, C_r is the reduced-dimensional (here, 1D in 2D domain) averaged elasticity tensor along the x direction and y direction boundary of the coarse element according to

$$\mathbf{C}_{\mathbf{r},\mathbf{x}} = \begin{bmatrix} \bar{\lambda} & 0 & 0 \\ 0 & 0 & 0 \\ 0 & 0 & \bar{\mu} \end{bmatrix}, \ \mathbf{C}_{\mathbf{r},\mathbf{y}} = \begin{bmatrix} 0 & 0 & 0 \\ 0 & \bar{\lambda} & 0 \\ 0 & 0 & \bar{\mu} \end{bmatrix}, \tag{29}$$

where, $\bar{\lambda}$ and $\bar{\mu}$ are the averaged Lamé parameters along the coarse scale element boundary. The basis function matrix P is composed of terms from x and y directions and has the form of

$$\mathbf{P} = \begin{bmatrix} P_{xx} & P_{xy} \\ P_{yx} & P_{yy} \end{bmatrix}. \tag{30}$$

To construct basis functions matrix algebraically, the stiffness matrix needs to be reordered. The reordered system allows to solve the Eq. (28) firstly, which is composed by only boundaries terms, and then the equilibrium equation Eq. (27) is solved. In Fig. 5, it is shown that all nodes in any coarse element can be split into three groups: internal, edge and vertex nodes. The fine-scale stiffness matrix $\mathbf{K}^h$ is permuted using the permutation operator $\mathbf{T}$ as

$$\begin{bmatrix} K_{II} & K_{IE} & K_{IV} \\ K_{EI} & K_{EE} & K_{EV} \\ K_{VI} & K_{VE} & K_{VV} \end{bmatrix} \begin{bmatrix} d_I \\ d_E \\ d_V \end{bmatrix} = \begin{bmatrix} f_I \\ f_E \\ f_V \end{bmatrix}. \tag{31}$$

Here, I represents the internal nodes, E represents the edge nodes and V represents the vertex nodes. The coarse-scale solutions can be computed based on the solutions on the vertex nodes. The functions that interpolate the solution between the vertex nodes through the edge and internal nodes are then the necessary basis functions.

The reduced-dimensional boundary condition Eq. (28) is now being imposed by a 1D XFEM discrete system in the 2D XFEM problem. This causes the entry K_{EI} to vanish, as the connectivity between the edge and internal nodes for the edge elements is assumed to disappear. This 1D edge equations can then be expressed as

$$K_{EE}^R d_E + K_{EV}^R d_V = 0. \tag{32}$$

Since the solutions at vertex nodes will be obtained from the coarse-scale system, the reordered fine-scale matrix can now be reduced to

$$\begin{bmatrix} K_{II} & K_{IE} & K_{IV} \\ 0 & K_{EE}^R & K_{EV}^R \\ 0 & 0 & K^H \end{bmatrix} \begin{bmatrix} d'_I \\ d'_E \\ d'_V \end{bmatrix} = \begin{bmatrix} 0 \\ 0 \\ f^H \end{bmatrix}, \tag{33}$$

where, the d'_I, d'_E and d'_V are the approximated displacements solutions for the internal nodes, edge nodes and vertex nodes. Note that the equations for basis functions do not consider source terms in their right-hand-side while these are transferred to the coarse scale system. Given the coarse nodes solutions d'_V, one can obtain the solution at the edge via

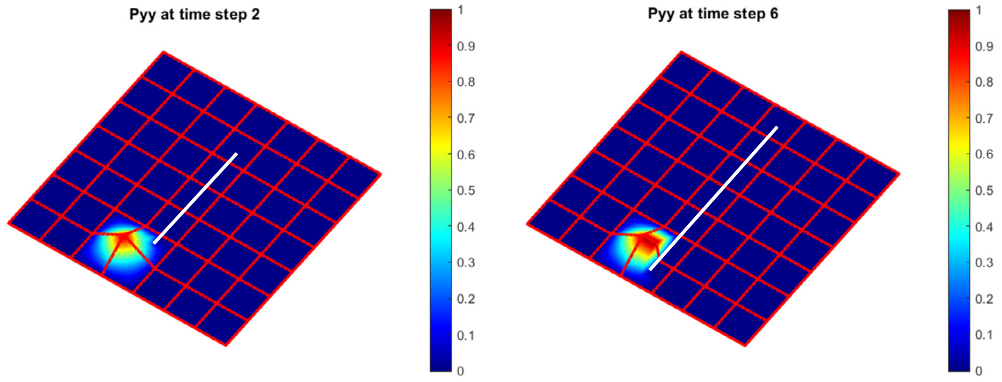

(a) (b)

Fig. 6. An example of updating the basis functions that captures the fracture growth from (a) step 2 to (b) step 6. The white segment represents the fracture.

Algorithm 1 Algorithm of MS-XFEM in fracture growth.

```
while Set of growing tips, $n_{grow}$, is not empty do
    Update stiffness matrix $K_f$
    Update $\mathbf{P}$ locally
    Update the MS-XFEM solutions: $d^h_{MS}$ iteratively
    Compute the $n_{grow}$ using double virtual incremental method
    Compute the growing angle $\theta$
    Update level sets functions: $\psi^t \to \psi^{t+1}$, $\phi^t \to \phi^{t+1}$
    Update fracture tip positions and enrichment
end while
```

$$d'_E = -(K^R_{EE})^{-1} K^R{}_{EV}\, d'_V = \mathbf{P}_{EV}\, d'_V. \tag{34}$$

Similarly, the solution at the internal cells reads

$$\begin{aligned} d'_I &= -K_{II}^{-1}(K_{IE} d'_E + K_{IV} d'_V) \\ &= -K_{II}^{-1}(-K_{IE}(K^R_{EE})^{-1} K^R{}_{EV} + K_{IV})\, d'_V = \mathbf{P}_{IV}\, d'_V. \end{aligned} \tag{35}$$

Note that $\mathbf{P}_{EV}$ and $\mathbf{P}_{IV}$ are the sub-matrices of the prolongation operator. The prolongation matrix is then defined as

$$\mathbf{d}' = \begin{bmatrix} d'_I \\ d'_E \\ d'_V \end{bmatrix} = \underbrace{\begin{bmatrix} P_{IV} \\ P_{EV} \\ I_{VV} \end{bmatrix}}_{\mathbf{P}} d'_V. \tag{36}$$

Here, I_{VV} is the diagonal identity matrix equal to the size of the number of vertex nodes.

After defining the prolongation operator algebraically, based on the entries of the 2D XFEM (for internal nodes) and 1D XFEM (for edge nodes), one can determine the multiscale solution.

4.3. MS-XFEM on fracture propagation

The propagation of fracture tips will change the geometries of fine scale discontinuities and these changes should be captured by the basis functions in MS-XFEM, as shown in Fig. 6. To be able to use MS-XFEM to simulate the fracture propagation, the basis functions need to be updated during each growth step. Note that it is not necessary to update the basis functions matrix globally since the fracture tips growth only affect the local coarse elements that contains this growing fracture tip or this fracture tip will propagate into.

Update of basis functions is straightforward with the algebraic method. In each growth step, the basis functions matrix is updated locally only on those coarse elements that are affected by the growing fracture tips. This is done by extracting the terms of the updated K_f matrix and reconstructing the local basis functions matrix P_l and reassemble P_l into global P matrix.

The Algorithm 1 shows the procedure how to use MS-XFEM simulate fractures propagation.

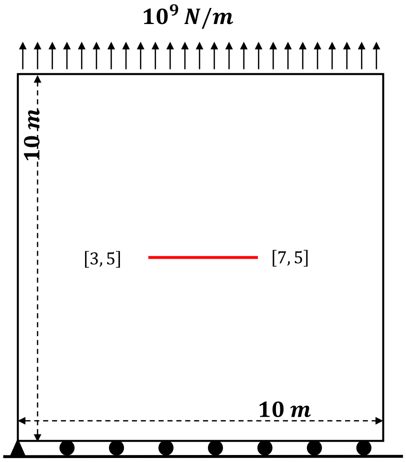

Fig. 7. Test case 1: illustration of the model setup.

When multiple fractures grow and cross each other, it is reasonable to apply adaptive local refinement around the crossing points or the fracture tips. This will improve the quality of the MS-XFEM results. A strategy such as ADM (adaptive dynamic multilevel) is a good option to be applied [57]. Currently these are not involved in this paper.

5. Numerical test cases

In this section both test cases have been performed to investigate the applicability of the MS-XFEM in simulation of single and multiple fractures propagation. For all test cases, a square 2D domain of 10 [m] × 10 [m] is considered. The material of both test cases is homogeneous sandstone with a Young's modulus $E = 25$ [GPa] and Poisson's ratio of 0.2. The fracture toughness of sandstone $K_c = 1.4 \times 10^6$ $[\mathrm{Pa} \cdot \mathrm{m}^{-\frac{1}{2}}]$ [58,59]. The fine scale mesh is set as 49 × 49 and the coarse mesh is 7 × 7 for both test cases. This results in a coarsening ratio of 7 × 7 in both x and y directions.

Both test cases are simulated using the MS-XFEM and compared with the fine scale results to check accuracy. To illustrate the importance of the iterative strategy on quality control, the result computed without using the iterative strategy, i.e., directly computed from (25), is shown. Also the result computed using preconditioned GMRES is shown. The criterion to stop the iterations is set as if the norm of the residual $||r^n||_2$ at current time step t^n is less than τ of the original residual norm $||r^0||_2$

$$\frac{||r^n||_2}{||r^0||_2} \leqslant \tau. \tag{37}$$

The tolerance input is affecting the number of iterations required to reach convergence. In this paper, two different tolerance values, $\tau = 10^{-8}$ and $\tau = 10^{-2}$, are applied. It is essential to observe how much improvement the iterative strategy can bring since this strategy will add extra computational burden. Normally there is no doubt that a tolerance of $\tau = 10^{-8}$ would give very accurate MS-XFEM solutions but it is also valuable to analyze whether the less accurate solutions ($\tau = 10^{-2}$) are acceptable since this less accurate solution has less computational burden.

5.1. Test case 1: homogeneous sandstone with single fracture

A single horizontal fracture test case as shown in Fig. 7 is simulated here. The fracture tip coordinates are shown in Fig. 7. The Dirichlet boundary conditions are applied at the bottom. The left-bottom corner is fixed in both x and y directions while the rest of the nodes at the bottom boundary are fixed only in y direction. At the top boundary, a distributed upward loading $q = 10^9$ [N/m] is applied. The left and right boundaries are set as stress free. The maximum step size that the fractures allowed to grow is 7 seconds, or 7 [s], and each time step is 1 [s]. In each step the length of the fracture increment is constant 0.4 [m].

Results for the displacement field without iterative strategy (Fig. 8(a)) and with the iterative strategy using an accuracy tolerance of $\tau = 10^{-2}$ (Fig. 8(b)) at the end of time step 4 are shown. The result for tolerance $\tau = 10^{-8}$ is not shown since it is nearly identical to the fine scale solution. Both MS-XFEM results (red color lines represent the coarse mesh 7 × 7) are plotted on top of the fine scale XFEM result (blue color using the mesh 49 × 49) in order to compare them.

Without the assistance of preconditioned GMRES, there is an obvious difference between the MS-XFEM solution compared to fine scale solution in Fig. 8 (a). The maximum difference between the displacements solutions is 0.22 [m]. This result properly captures the opening of the fracture. The MS-XFEM result with error tolerance $\tau = 10^{-2}$ is very close to the

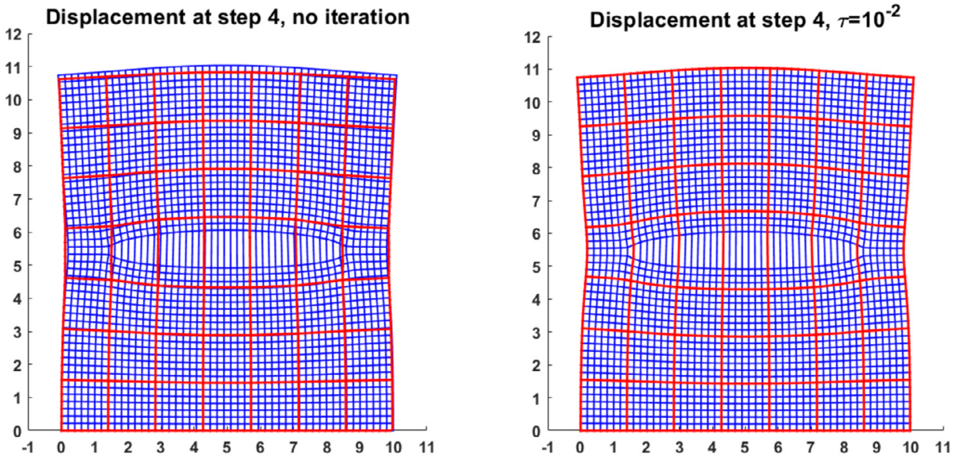

(a) (b)

Fig. 8. Test Case 1: displacement field at time step 4 using (a) no iterative strategy and (b) tolerance $\tau = 10^{-2}$ with 11 iterations to reach convergence. Red lines represent the coarse scale mesh with MS-XFEM displacement field plotted on coarse scale grid. Blue lines represent the fine scale mesh with fine scale solution plotted on fine scale grid.

fine scale XFEM result. The number of iterations required for Fig. 8 (b) is 11 while the iterations for obtaining the solution with tolerance $\tau = 10^{-8}$ is 34 which implies more computational costs.

The crack path from initial step to final step is tracked and at time step 4 and 6 the crack patterns are plotted in Fig. 9. The crack angle is computed using Eq. (12). The two crack paths are computed using the MS-XFEM displacement solutions that computed without iterative strategy and with the iterative strategy using the tolerance of $\tau = 10^{-2}$. These two crack paths are both compared with the crack path computed based on the fine scale displacement field. Note that the crack paths predicted using fine scale XFEM solutions are plotted in blue color. It is clear that using the iterative strategy or not yields the same crack path considering that this is a pure mode I problem of single fracture. For complicated fracture systems as for the next test case, this is not true.

The convergence characteristic at step 2, 4 and 6 using preconditioned GMRES is shown in Fig. 10. The number of extra DOFs involved in these three steps are: 112, 144 and 176, respectively. The number of iterations to reach convergence with respect to a tolerance of 10^{-8} of these three steps are: 32, 34 and 36. Thus the iterations required to reach convergence are slightly increasing with the growth of fractures. This is reasonable since growing fractures increase the number of extra DOFs.

5.2. Test case 2: homogeneous sandstone with multiple fractures

The second test case is used to test the application of MS-XFEM in the simulation of multiple fractures propagation. The fractures setup is shown in Fig. 11. The fractures are rotated around its center point (marked with red circle). The coordinates of center points of each fracture and the rotation angles are shown in brackets. The four fractures been labeled with a number from 1 to 4. The initial length of each fracture is all 1 [m]. Number of maximum growing step size is set as 17 [s] and each time step size is 1 [s]. The fracture increment is set as 0.4 [m] per time step. The Dirichlet boundary conditions are applied at the bottom. The bottom center point is fixed in both x and y directions while the rest of the nodes along bottom boundary are fixed in y direction. At the top a distributed upward loading $q = 10^7$ [N/m] is applied. The left and right boundaries are set as stress free.

If no GMRES is used to control the error level of final solutions, the MS-XFEM fails to predict the crack path as shown in Fig. 12. This suggests that the errors accumulated in highly fractured system will become too significant to ignore them and thus the iterative strategy is necessary to be paired with MS-XFEM. In the following, only the test case using GMRES with tolerance of $\tau = 10^{-2}$ is studied.

The propagation crack paths at step 4, 10 and 15 are shown in the upper row of Fig. 13. It is clear that not all tips will grow considering the global minimum energy release by Eq. (21). Since the preconditioned GMRES is applied, displacement field solutions from MS-XFEM are close to the fine scale XFEM solutions, which is shown in the bottom row of Fig. 13.

However, there is still small difference between the predicted crack pattern in step 15, which is shown in the top right part of Fig. 13 (c). This is due to the generous tolerance $\tau = 10^{-2}$ given in here. When the tolerance is set as high as $\tau = 10^{-8}$, the accuracy of MS-XFEM result is very high as shown in Fig. 14. But the iteration number required to reach $\tau = 10^{-8}$ is 53 while it only requires 28 iterations to reach $\tau = 10^{-2}$. Considering the less computational burden, the result of Fig. 13 (c) is still considered as good prediction.

The stress plots are shown in the lower row of Fig. 13, which partly reveals why some tips grow and others do not. The sequence of propagating crack tips is as follows. First, both the two tips of fracture 3 grows since the maximum stress is

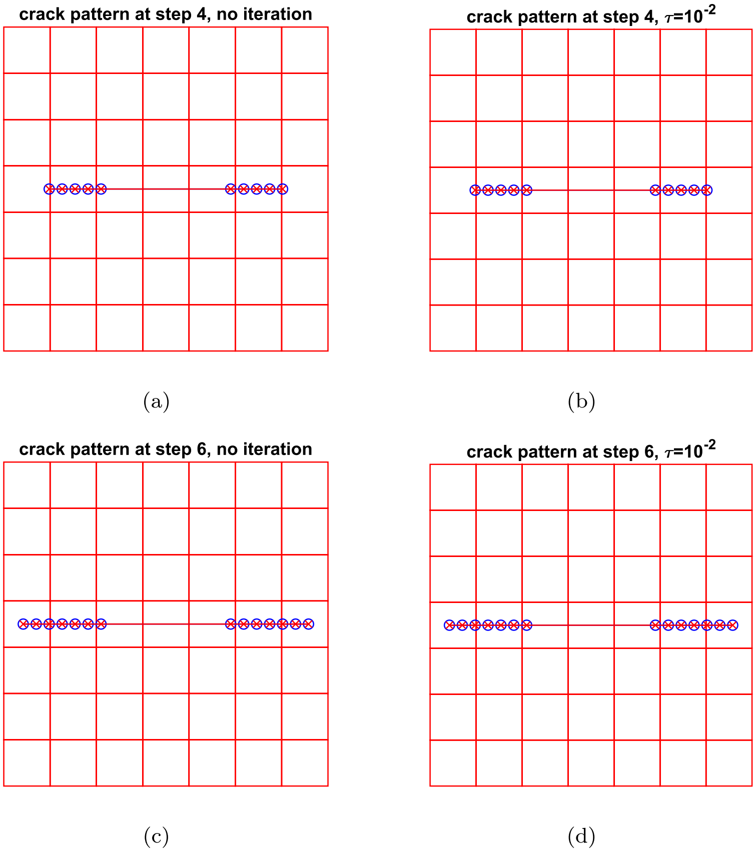

(a) (b) (c) (d)

Fig. 9. Test case 1: fracture propagation path at step 4 and 6. Red lines represent the coarse scale mesh. Blue segments and blue circles represent the fine scale fracture path while red segments and red crosses represent the path predicted using MS-XFEM. The left column includes the paths predicted using MS-XFEM without iterations. The right column includes the paths predicted using MS-XFEM with tolerance of 10^{-2}.

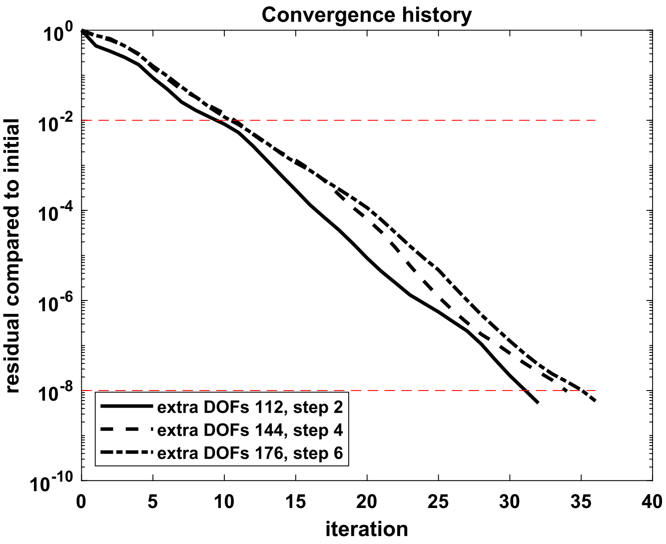

Fig. 10. Test case 1: convergence history at step 2, 4 and 6 using preconditioned GMRES. The corresponding extra DOFs are: 112, 144 and 176. The number of iterations to reach convergence is increasing as fracture is growing.

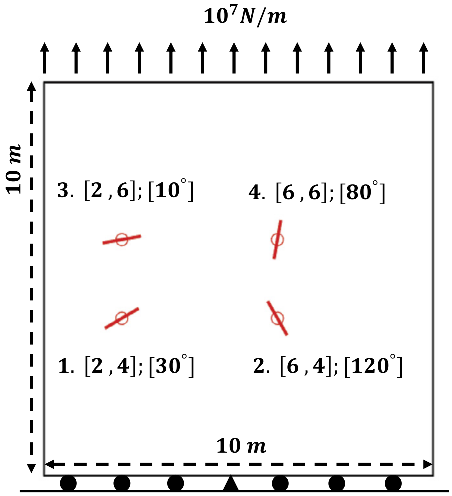

Fig. 11. Test case 2: Multiple fractures within a homogeneous sandstone sample under tension stress.

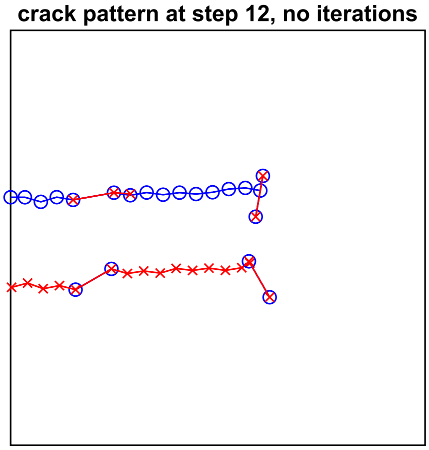

Fig. 12. Test case 2: crack pattern predicted at step 12. The blue curve represents the crack path predicted using only the fine scale solution and the red curves represent the incorrect crack paths predicted using MS-XFEM solution.

located around both tips of fracture 3, as shown in Fig. 13 (d). At step 9, the left tip of fracture 3 reaches at the left edge of domain. Then the right tip of fracture 3 propagates since the maximum stress surrounds this tip as shown in 13 (e). At step 12, the right tip of fracture 3 grows and joins fracture 4. After that, the top fracture tip of fracture 4 continues to grow, which is represented in Fig. 13 (f) since the top fracture tip is located in the peak stress area.

The convergence characteristics, recorded using preconditioned GMRES, are shown in Fig. 15. In this figure, the convergence characteristics at step 4, 10 and 15 are plotted. Extra DOFs for each of these steps, respectively, are: 136, 192 and 248. The iterations required to reach convergence with respect to the tolerance of 10^{-8} are: 38, 46 and 53, respectively. Clearly, the number of iterations required to reach convergence is increasing as the fractures are growing.

6. Conclusion

An adaptive multiscale method for XFEM, namely MS-XFEM, is proposed to track the propagation of multiple fractures in geological formations. The growth of fractures leads to the extension and also the junction of discontinuities. The basis functions are capable of capturing this extension or junction of the fine scale fractures. The basis functions are updated in an algebraic manner based on the updated fine-scale stiffness matrix, which is revised in accordance with the growth of fractures. This makes MS-XFEM suitable to simulate propagation of fractures. With the assistance of preconditioned GMRES, the quality of the displacement field result is controlled to a certain level of accuracy, which ensures the correct prediction of fractures growth in the next step. Test cases results show that MS-XFEM with preconditioned GMRES track the growth of fractures paths correctly, even if the error tolerance is not extremely small. This means that the basis functions successfully capture the changes of these fractures.

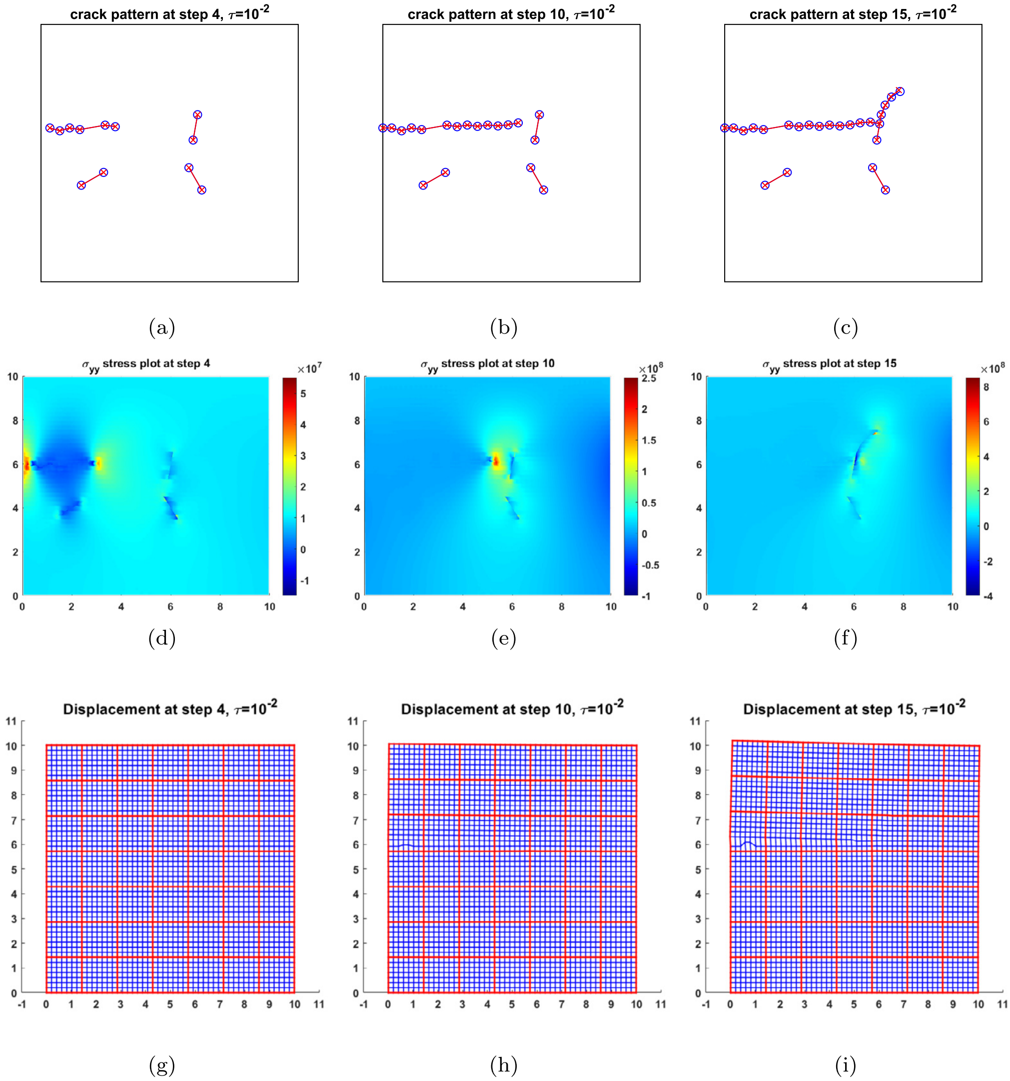

Fig. 13. Test case 2: crack paths growing history at step 4, 10 and 15. Upper row includes crack patterns predicted. Red segments and crosses represent crack paths predicted using MS-XFEM result and blue segments and circles represent the crack paths predicted using fine scale XFEM result. The middle row includes the stress plot of σ_{yy} at these steps. The bottom row includes the displacement field solutions by fine scale XFEM (blue) and MS-XFEM (red).

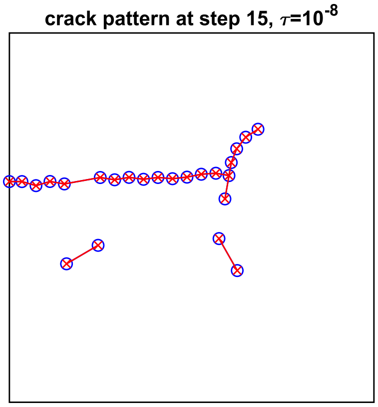

Fig. 14. Test case 2: crack pattern predicted at step 15 using tolerance value of 10^{-8}. The blue curve represents the crack path predicted using only the fine scale solution and the red curves represent the correct crack paths predicted using MS-XFEM solution. 53 iterations required to reach this accuracy while only 28 iterations required to reach $\tau = 10^{-2}$.

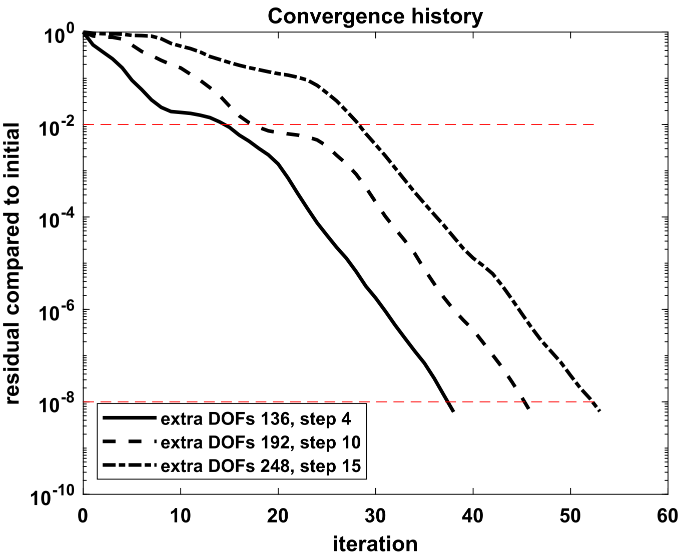

Fig. 15. Test case 2: convergence history using preconditioned GMRES. The number of extra DOFs at steps 4, 10 and 15, respectively, are: 136, 192 and 248. The number of iterations to reach convergence is increasing with the growth of fractures.

CRediT authorship contribution statement

Fanxiang Xu: Conceptualization, Methodology, Software, Writing – original draft. **Hadi Hajibeygi:** Conceptualization, Methodology, Supervision, Writing – review & editing. **Lambertus J. Sluys:** Conceptualization, Methodology, Supervision, Writing – review & editing.

Declaration of competing interest

The authors declare the following financial interests/personal relationships which may be considered as potential competing interests: Fanxiang Xu reports financial support was provided by China Scholarship Council (grant number 201807720039).

Data availability

Data will be made available on request.

Acknowledgements

Fanxiang Xu is sponsored by the China Scholarship Council (CSC, grant number 201807720039). Authors acknowledge all members of the Delft Advanced Reservoir Simulation (DARSim) group, ADMIRE research group and computational mechanics group. Special thanks to Dr. N. Castelletto and Prof. C. Vuik for their valuable discussions and suggestions.

References

[1] E.L. Majer, R. Baria, M. Stark, S. Oates, J. Bommer, B. Smith, H. Asanuma, Induced seismicity associated with enhanced geothermal systems, Geothermics 36 (3) (2007) 185–222.
[2] T. Postma, J.-D. Jansen, The small effect of poroelastic pressure transients on triggering of production-induced earthquakes in the Groningen natural gas field, J. Geophys. Res., Solid Earth 123 (jan 2018) 401–417.
[3] S. Krevor, H. de Coninck, S. Gasda, N.S. Ghaleigh, V. de Gooyert, H. Hajibeygi, R. Juanes, J. Neufeld, J. Roberts, F. Swennenhuis, Algebraic dynamic multilevel method for compositional flow in heterogeneous porous media, Nat. Rev. Earth Environ. 4 (2023) 102–118.
[4] A.A. Griffith, VI. the phenomena of rupture and flow in solids, Philos. Trans. R. Soc. Lond., Ser. A, Contain. Pap. Math. Phys. Character 221 (jan 1921) 163–198.
[5] F. Erdogan, G.C. Sih, On the crack extension in plates under plane loading and transverse shear, J. Basic Eng. 85 (dec 1963) 519–525.
[6] X.-Z. Suo, A. Combescure, Double virtual crack extension method for crack growth stability assessment, Int. J. Fract. 57 (2) (1992) 127–150.
[7] É. Budyn, G. Zi, N. Moës, T. Belytschko, A method for multiple crack growth in brittle materials without remeshing, Int. J. Numer. Methods Eng. 61 (sep 2004) 1741–1770.
[8] T. Belytschko, Y.Y. Lu, L. Gu, Element-free Galerkin methods, Int. J. Numer. Methods Eng. 37 (jan 1994) 229–256.
[9] N. Moes, J. Dolbow, T. Belytschko, A finite element method for crack growth without remeshing, Int. J. Numer. Methods Eng. 46 (sep 1999) 131–150.
[10] M. Rashid, The arbitrary local mesh replacement method: an alternative to remeshing for crack propagation analysis, Comput. Methods Appl. Mech. Eng. 154 (feb 1998) 133–150.

[11] T. Bittencourt, P. Wawrzynek, A. Ingraffea, J. Sousa, Quasi-automatic simulation of crack propagation for 2d lefm problems, Eng. Fract. Mech. 55 (09 1996) 321–334.
[12] J. Jiang, R.M. Younis, Hybrid coupled discrete-fracture/matrix and multicontinuum models for unconventional-reservoir simulation, SPE J. 21 (2016) 1009–1027.
[13] T.T. Garipov, P. Tomin, R. Rin, D.V. Voskov, H.A. Tchelepi, Unified thermo-compositional-mechanical framework for reservoir simulation, Comput. Geosci. 22 (4) (2018) 1039–1057.
[14] Y. Wang, M. Shahvali, Discrete fracture modeling using centroidal Voronoi grid for simulation of shale gas plays with coupled nonlinear physics, Fuel 163 (jan 2016) 65–73.
[15] A. Novikov, D. Voskov, M. Khait, H. Hajibeygi, J.D. Jansen, A scalable collocated finite volume scheme for simulation of induced fault slip, J. Comput. Phys. 469 (2022) 111598.
[16] H. Hajibeygi, D. Karvounis, P. Jenny, A hierarchical fracture model for the iterative multiscale finite volume method, J. Comput. Phys. 230 (2011) 8729–8743.
[17] M. Tene, S.B. Bosma, M.S.A. Kobaisi, H. Hajibeygi, Projection-based embedded discrete fracture model (pEDFM), Adv. Water Resour. 105 (jul 2017) 205–216.
[18] A.R. Khoei, M. Vahab, E. Haghighat, S. Moallemi, A mesh-independent finite element formulation for modeling crack growth in saturated porous media based on an enriched-FEM technique, Int. J. Fract. 188 (jun 2014) 79–108.
[19] Y. Efendiev, J. Galvis, G. Li, M. Presho, Generalized multiscale finite element methods. oversampling strategies, Int. J. Multiscale Comput. Eng. 12 (6) (2014) 465–484.
[20] J.Y. Wu, F. Li, An improved stable XFEM (is-XFEM) with a novel enrichment function for the computational modeling of cohesive cracks, Comput. Methods Appl. Mech. Eng. 295 (oct 2015) 77–107.
[21] T. Belytschko, T. Black, Elastic crack growth in finite elements with minimal remeshing, Int. J. Numer. Methods Eng. 45 (5) (1999) 601–620.
[22] A.M. Aragón, A. Simone, The discontinuity-enriched finite element method, Int. J. Numer. Methods Eng. 112 (sep 2017) 1589–1613.
[23] F.P. Meer, L.J. Sluys, A phantom node formulation with mixed mode cohesive law for splitting in laminates, Int. J. Fract. 158 (may 2009) 107–124.
[24] K. Amir R, Extended Finite Element Method: Theory and Applications, John Wiley & Sons, Incorporated, 2015.
[25] C. Daux, N. Moës, J. Dolbow, N. Sukumar, T. Belytschko, Arbitrary branched and intersecting cracks with the extended finite element method, Int. J. Numer. Methods Eng. 48 (12) (2000) 1741–1760.
[26] S.S. Behbahani, H. Hajibeygi, D. Voskov, J.D. Jansen, Smoothed embedded finite-volume method (sefvm) for modeling contact mechanics in deformable faulted and fractured porous media, J. Comput. Phys. 459 (2022) 111143.
[27] J. Melenk, I. Babuška, The partition of unity finite element method: basic theory and applications, Comput. Methods Appl. Mech. Eng. 139 (1) (1996) 289–314.
[28] S. Osher, J.A. Sethian, Fronts propagating with curvature-dependent speed: algorithms based on Hamilton-Jacobi formulations, J. Comput. Phys. 79 (nov 1988) 12–49.
[29] M. Stolarska, D.L. Chopp, N. Moës, T. Belytschko, Modelling crack growth by level sets in the extended finite element method, Int. J. Numer. Methods Eng. 51 (jul 2001) 943–960.
[30] G. Allaire, Homogenization and two-scale convergence, SIAM J. Math. Anal. 23 (6) (1992) 1482–1518.
[31] A. Abdulle, E. Weinan, Finite difference heterogeneous multi-scale method for homogenization problems, J. Comput. Phys. 191 (1) (2003) 18–39.
[32] Y. Amanbek, G. Singh, M.F. Wheeler, H. van Duijn, Adaptive numerical homogenization for upscaling single phase flow and transport, J. Comput. Phys. 387 (2019) 117–133.
[33] U. Hornung, Homogenization and Porous Media, vol. 6, Springer Science & Business Media, 1997.
[34] K. Kumar, T. van Noorden, I.S. Pop, Upscaling of reactive flows in domains with moving oscillating boundaries, Discrete Contin. Dyn. Syst. 7 (2014) 623–644.
[35] H.-W. Zhang, J.-K. Wu, J. Lü, Z.-D. Fu, Extended multiscale finite element method for mechanical analysis of heterogeneous materials, Acta Mech. Sin. 26 (dec 2010) 899–920.
[36] R. Patil, B. Mishra, I. Singh, A new multiscale XFEM for the elastic properties evaluation of heterogeneous materials, Int. J. Mech. Sci. 122 (mar 2017) 277–287.
[37] A. Khoei, M. Hajiabadi, Fully coupled hydromechanical multiscale model with microdynamic effects, Int. J. Numer. Methods Eng. 115 (apr 2018) 293–327.
[38] M.R. Hajiabadi, A.R. Khoei, A bridge between dual porosity and multiscale models of heterogeneous deformable porous media, Int. J. Numer. Anal. Methods Geomech. 43 (oct 2018) 212–238.
[39] H. Hajibeygi, P. Jenny, Multiscale finite-volume method for parabolic problems arising from compressible multiphase flow in porous media, J. Comput. Phys. 228 (aug 2009) 5129–5147.
[40] N. Castelletto, H. Hajibeygi, H.A. Tchelepi, Multiscale finite-element method for linear elastic geomechanics, J. Comput. Phys. 331 (feb 2017) 337–356.
[41] I. Sokolova, M.G. Bastisya, H. Hajibeygi, Multiscale finite volume method for finite-volume-based simulation of poroelasticity, J. Comput. Phys. 379 (feb 2019) 309–324.
[42] P. Jenny, S. Lee, H. Tchelepi, Multi-scale finite-volume method for elliptic problems in subsurface flow simulation, J. Comput. Phys. 187 (may 2003) 47–67.
[43] R. Deb, P. Jenny, Finite volume-based modeling of flow-induced shear failure along fracture manifolds, Int. J. Numer. Anal. Methods Geomech. 41 (jul 2017) 1922–1942.
[44] N. Castelletto, H. Hajibeygi, H. Tchelepi, Hybrid multiscale formulation for coupled flow and geomechanics, in: ECMOR XV - 15th European Conference on the Mathematics of Oil Recovery, EAGE Publications BV, aug 2016.
[45] B. Giovanardi, L. Formaggia, A. Scotti, P. Zunino, Unfitted FEM for modelling the interaction of multiple fractures in a poroelastic medium, in: Lecture Notes in Computational Science and Engineering, Springer International Publishing, 2017, pp. 331–352.
[46] H. Hajibeygi, G. Bonfigli, M.A. Hesse, P. Jenny, Iterative multiscale finite-volume method, J. Comput. Phys. 227 (oct 2008) 8604–8621.
[47] Y. Wang, H. Hajibeygi, H.A. Tchelepi, Algebraic multiscale solver for flow in heterogeneous porous media, J. Comput. Phys. 259 (2014) 284–303.
[48] E.T. Chung, Y. Efendiev, G. Li, An adaptive gmsfem for high-contrast flow problems, J. Comput. Phys. 273 (2014) 54–76.
[49] S. Loehnert, T. Belytschko, A multiscale projection method for macro/microcrack simulations, Int. J. Numer. Methods Eng. 71 (12) (2007) 1466–1482.
[50] M. Holl, S. Loehnert, P. Wriggers, An adaptive multiscale method for crack propagation and crackcoalescence, Int. J. Numer. Methods Eng. 93 (jun 2012) 23–51.
[51] F. Xu, H. Hajibeygi, L.J. Sluys, Multiscale extended finite element method for deformable fractured porous media, J. Comput. Phys. 436 (jul 2021) 110287.
[52] J. Lemaitre, J.-L. Chaboche, Mechanics of Solid Materials, Cambridge University Press, 1994.
[53] H. Wang, Theory of Linear Poroelasticity with Applications to Geomechanics and Hydrogeology, Princeton Series in Geophysics, Princeton University Press, 2017.
[54] R.D. Cook, et al., Concepts and Applications of Finite Element Analysis, John Wiley & Sons, 2007.

[55] Y. Saad, M.H. Schultz, GMRES: a generalized minimal residual algorithm for solving nonsymmetric linear systems, SIAM J. Sci. Stat. Comput. 7 (3) (1986) 856–869.
[56] E. Chow, Y. Saad, Experimental study of ILU preconditioners for indefinite matrices, J. Comput. Appl. Math. 86 (dec 1997) 387–414.
[57] M. Cusini, B. Fryer, C. van Kruijsdijk, H. Hajibeygi, Algebraic dynamic multilevel method for compositional flow in heterogeneous porous media, J. Comput. Phys. 354 (feb 2018) 593–612.
[58] D. Huang, B. Li, W. Ma, D. Cen, Y. Song, Effects of bedding planes on fracture behavior of sandstone under semi-circular bending test, Theor. Appl. Fract. Mech. 108 (aug 2020) 102625.
[59] P. Senseny, T. Pfeifle, Fracture toughness of sandstones and shales, 1984.